

CMOS-compatible mid-IR metamaterial absorbers for out-of-band suppression in optical MEMS

Ghaderi, Amir; Karimishahmarvandi, Ehsan; Wolfenbuttel, Reinoud

DOI

[10.1364/OME.8.001696](https://doi.org/10.1364/OME.8.001696)

Publication date

2018

Document Version

Publisher's PDF, also known as Version of record

Published in

Optical Materials Express

Citation (APA)

Ghaderi, M., Karimi Shahmarvandi, E., & Wolfenbuttel, R. F. (2018). CMOS-compatible mid-IR metamaterial absorbers for out-of-band suppression in optical MEMS. *Optical Materials Express*, 8(7), 1696-1707. DOI: 10.1364/OME.8.001696

Important note

To cite this publication, please use the final published version (if applicable). Please check the document version above.

Copyright

Other than for strictly personal use, it is not permitted to download, forward or distribute the text or part of it, without the consent of the author(s) and/or copyright holder(s), unless the work is under an open content license such as Creative Commons.

Takedown policy

Please contact us and provide details if you believe this document breaches copyrights. We will remove access to the work immediately and investigate your claim.



CMOS-compatible mid-IR metamaterial absorbers for out-of-band suppression in optical MEMS

MOHAMMADAMIR GHADERI,* EHSAN KARIMI SHAHMARVANDI,
AND REINOUD F. WOLFFENBUTTEL

Electronic Instrumentation Laboratory, Department of Microelectronics, Delft University of Technology, 2628 CD, Delft, the Netherlands

*m.ghaderi@tudelft.nl

Abstract: The design and fabrication of wideband mid-infrared metamaterial absorbers are presented. The emphasis is put on the shape-tolerant design for using masked UV (i-line) lithography and CMOS-compatible fabrication to enable on-chip co-integration with detector and readout circuits in a MEMS foundry while maintaining wafer throughput. The CMOS-compatibility implies the use of aluminum rather than the commonly used high conductivity metals. The use of masked lithography rather than e-beam lithography in the fabrication of metamaterial absorbers for the mid-infrared range between 3 and 4 μm introduces the challenge of the shape-tolerant design of the unit cell. Moreover, the sensitivity of the fabricated metamaterials to the surface roughness and exposure dose were investigated in this paper. The throughput advantage of masked lithography has been exploited in the fabrication of mid-infrared absorbers over an area of several mm^2 . The measurements confirm the theoretical spectral response and a 98% peak absorption at an angle close to perpendicular incidence. Measurements at different angles show that the absorption spectrum only deviates marginally from normal incidence for angles up to 30° . The combined CMOS-compatibility and masked lithography enable batch fabrication and the on-chip integration of the metamaterial absorbers with MEMS devices and sensors.

© 2018 Optical Society of America under the terms of the [OSA Open Access Publishing Agreement](#)

OCIS codes: (160.3918) Metamaterials; (230.4000) Microstructure fabrication; (230.4685) Optical microelectromechanical devices.

References and links

1. R. F. Wolffebuttel, "MEMS-based optical mini- and microspectrometers for the visible and infrared spectral range," *J. Micromech. Microeng.* **15**(7), S145–S152 (2005).
2. S. Gersen, M. van Essen, G. van Dijk, and H. Levinsky, "Physicochemical effects of varying fuel composition on knock characteristics of natural gas mixtures," *Combust. Flame* **161**(10), 2729–2737 (2014).
3. N. P. Ayerden, G. de Graaf, and R. F. Wolffebuttel, "Compact gas cell integrated with a linear variable optical filter," *Opt. Express* **24**(3), 2981–3002 (2016).
4. M. Ghaderi, N. P. Ayerden, A. Emadi, P. Enoksson, J. H. Correia, G. Graaf, and R. F. Wolffebuttel, "Design, fabrication and characterization of infrared LVOFs for measuring gas composition," *J. Micromech. Microeng.* **24**(8), 084001 (2014).
5. A. Emadi, H. Wu, G. de Graaf, and R. Wolffebuttel, "Design and implementation of a sub-nm resolution microspectrometer based on a Linear-Variable Optical Filter," *Opt. Express* **20**(1), 489–507 (2012).
6. A. Emadi, H. Wu, S. Grabarnik, G. Graaf, and R. F. Wolffebuttel, "Vertically tapered layers for optical applications fabricated using resist reflow," *J. Micromech. Microeng.* **19**(7), 074014 (2009).
7. "Optical filter guide www.spectrofilm.com/optical-filter-guide-spectrofilm.pdf.
8. R. F. Wolffebuttel, "Optical Sensors Based on Photon Detection," in *Smart Sensor Systems*, G. C. M. Meijer, ed. (Wiley, 2008), pp. 79–120.
9. A. D. Parsons and D. J. Pedder, "Thin-film infrared absorber structures for advanced thermal detectors," *J. Vac. Sci. Technol. A* **6**(3), 1686–1689 (1988).
10. S. Shu, Z. Li, and Y. Y. Li, "Triple-layer Fabry-Perot absorber with near-perfect absorption in visible and near-infrared regime," *Opt. Express* **21**(21), 25307–25315 (2013).
11. M. A. Kats and F. Capasso, "Optical absorbers based on strong interference in ultra-thin films," *Laser Photonics Rev.* **10**(5), 735–749 (2016).

12. H. Wu, A. Emadi, P. M. Sarro, G. Graaf, and R. F. Wolffenbuttel, "A surface micromachined thermopile detector array with an interference-based absorber," *J. Micromech. Microeng.* **21**(7), 074009 (2011).
13. L. John, T. Evangelos, E. George, and P. Chris, "Gold-black coatings for freestanding pyroelectric detectors," *Meas. Sci. Technol.* **14**(7), 916–922 (2003).
14. A. Y. Vorobyev and C. Guo, "Metallic Light Absorbers Produced by Femtosecond Laser Pulses," *Adv. Mech. Eng.* **2**, 452749 (2010).
15. M. Hirota, Y. Nakajima, M. Saito, and M. Uchiyama, "120×90 element thermoelectric infrared focal plane array with precisely patterned Au-black absorber," *Sens. Actuators A Phys.* **135**(1), 146–151 (2007).
16. W. Lang, K. Kühn, and H. Sandmaier, "Absorbing layers for thermal infrared detectors," *Sens. Actuators A Phys.* **34**(3), 243–248 (1992).
17. V. J. Gokhale, O. A. Shenderova, G. E. McGuire, and M. Rais-Zadeh, "Infrared Absorption Properties of Carbon Nanotube/Nanodiamond Based Thin Film Coatings," *J. Microelectromech. Syst.* **23**(1), 191–197 (2014).
18. J. H. Lehman, C. Engtrakul, T. Gennett, and A. C. Dillon, "Single-wall carbon nanotube coating on a pyroelectric detector," *Appl. Opt.* **44**(4), 483–488 (2005).
19. H. Wu, S. Vollebregt, A. Emadi, G. de Graaf, R. Ishihara, and R. F. Wolffenbuttel, "Use of multi-wall carbon nanotubes as an absorber in a thermal detector," *Procedia Eng.* **25**, 523–526 (2011).
20. Y. P. Lee, J. Y. Rhee, Y. J. Yoo, and K. W. Kim, *Metamaterials for perfect absorption* (Springer, 2016), Vol. **236**.
21. B. M. Adomanis, C. M. Watts, M. Koirala, X. Liu, T. Tyler, K. G. West, T. Starr, J. N. Bringuier, A. F. Starr, N. M. Jokerst, and W. J. Padilla, "Bi-layer metamaterials as fully functional near-perfect infrared absorbers," *Appl. Phys. Lett.* **107**(2), 021107 (2015).
22. X. Liu, T. Starr, A. F. Starr, and W. J. Padilla, "Infrared Spatial and Frequency Selective Metamaterial with Near-Unity Absorbance," *Phys. Rev. Lett.* **104**(20), 207403 (2010).
23. B. Zhang, J. Hendrickson, and J. Guo, "Multispectral near-perfect metamaterial absorbers using spatially multiplexed plasmon resonance metal square structures," *J. Opt. Soc. Am. B* **30**(3), 656–662 (2013).
24. C.-W. Cheng, M. N. Abbas, C.-W. Chiu, K.-T. Lai, M.-H. Shih, and Y.-C. Chang, "Wide-angle polarization independent infrared broadband absorbers based on metallic multi-sized disk arrays," *Opt. Express* **20**(9), 10376–10381 (2012).
25. N. Liu, H. Guo, L. Fu, S. Kaiser, H. Schweizer, and H. Giessen, "Three-dimensional photonic metamaterials at optical frequencies," *Nat. Mater.* **7**(1), 31–37 (2008).
26. E. K. Shahmarvandi, M. Ghaderi, N. P. Ayerden, G. d. Graaf, and R. F. Wolffenbuttel, "CMOS-compatible metamaterial-based wideband mid-infrared absorber for microspectrometer applications," in *SPIE Photonics Europe*, (SPIE, 2016), 9.
27. M. Ghaderi, E. Karimi, N. P. Ayerden, and R. F. Wolffenbuttel, "Fabrication Tolerance Sensitivity in Large-Area Mid-Infrared Metamaterial Absorbers," *Proceedings* **1**(4), 328 (2017).
28. T. Maier and H. Brueckl, "Multispectral microbolometers for the midinfrared," *Opt. Lett.* **35**(22), 3766–3768 (2010).
29. Y. Li, D. Li, C. Chi, and B. Huang, "Achieving Strong Field Enhancement and Light Absorption Simultaneously with Plasmonic Nanoantennas Exploiting Film-Coupled Triangular Nanodisks," *J. Phys. Chem. C* **121**(30), 16481–16490 (2017).
30. R. Alaei, C. Menzel, U. Huebner, E. Pshenay-Severin, S. Bin Hasan, T. Pertsch, C. Rockstuhl, and F. Lederer, "Deep-Subwavelength Plasmonic Nanoresonators Exploiting Extreme Coupling," *Nano Lett.* **13**(8), 3482–3486 (2013).
31. M. J. Dicken, K. Aydin, I. M. Pryce, L. A. Sweatlock, E. M. Boyd, S. Walavalkar, J. Ma, and H. A. Atwater, "Frequency tunable near-infrared metamaterials based on VO₂ phase transition," *Opt. Express* **17**(20), 18330–18339 (2009).
32. J. A. Montoya, Z.-B. Tian, S. Krishna, and W. J. Padilla, "Ultra-thin infrared metamaterial detector for multicolor imaging applications," *Opt. Express* **25**(19), 23343–23355 (2017).
33. G. V. Naik, J. L. Schroeder, X. Ni, A. V. Kildishev, T. D. Sands, and A. Boltasseva, "Titanium nitride as a plasmonic material for visible and near-infrared wavelengths," *Opt. Mater. Express* **2**(4), 478–489 (2012).
34. I. Sersic, M. Frimmer, E. Verhagen, and A. F. Koenderink, "Electric and Magnetic Dipole Coupling in Near-Infrared Split-Ring Metamaterial Arrays," *Phys. Rev. Lett.* **103**(21), 213902 (2009).
35. S. L. Wadsworth, P. G. Clem, E. D. Branson, and G. D. Boreman, "Broadband circularly-polarized infrared emission from multilayer metamaterials," *Opt. Mater. Express* **1**(3), 466–479 (2011).
36. Y. Wang, A. C. Overvig, S. Shrestha, R. Zhang, R. Wang, N. Yu, and L. Dal Negro, "Tunability of indium tin oxide materials for mid-infrared plasmonics applications," *Opt. Mater. Express* **7**(8), 2727–2739 (2017).
37. N. Liu, M. Mesch, T. Weiss, M. Hentschel, and H. Giessen, "Infrared Perfect Absorber and Its Application As Plasmonic Sensor," *Nano Lett.* **10**(7), 2342–2348 (2010).
38. I. Faniayeu and V. Mizeikis, "Realization of a helix-based perfect absorber for IR spectral range using the direct laser write technique," *Opt. Mater. Express* **7**(5), 1453–1462 (2017).
39. B. Barho Franziska, F. Gonzalez-Posada, M.-J. Milla, M. Bomers, L. Cerutti, E. Tournié, and T. Taliercio, "Highly doped semiconductor plasmonic nanoantenna arrays for polarization selective broadband surface-enhanced infrared absorption spectroscopy of vanillin," in *Nanophotonics*, (2017), p. 507.
40. S. Ogawa, Y. Takagawa, and M. Kimata, "Broadband polarization-selective uncooled infrared sensors using tapered plasmonic micrograting absorbers," *Sens. Actuators A Phys.* **269**, 563–568 (2018).

41. S. Ogawa, D. Fujisawa, H. Hata, M. Uetsuki, K. Misaki, and M. Kimata, "Mushroom plasmonic metamaterial infrared absorbers," *Appl. Phys. Lett.* **106**(4), 041105 (2015).
42. J. Y. Suen, K. Fan, J. Montoya, C. Bingham, V. Stenger, S. Sriram, and W. J. Padilla, "Multifunctional metamaterial pyroelectric infrared detectors," *Optica* **4**(2), 276–279 (2017).
43. L. Yang, P. Zhou, T. Huang, G. Zhen, L. Zhang, L. Bi, X. Weng, J. Xie, and L. Deng, "Broadband thermal tunable infrared absorber based on the coupling between standing wave and magnetic resonance," *Opt. Mater. Express* **7**(8), 2767–2776 (2017).
44. K. Üstün and G. Turhan-Sayan, "Wideband long wave infrared metamaterial absorbers based on silicon nitride," *J. Appl. Phys.* **120**(20), 203101 (2016).
45. A. D. Rakić, A. B. Djurišić, J. M. Elazar, and M. L. Majewski, "Optical properties of metallic films for vertical-cavity optoelectronic devices," *Appl. Opt.* **37**(22), 5271–5283 (1998).
46. N. Liu, L. Fu, S. Kaiser, H. Schweizer, and H. Giessen, "Plasmonic Building Blocks for Magnetic Molecules in Three-Dimensional Optical Metamaterials," *Adv. Mater.* **20**(20), 3859–3865 (2008).

1. Introduction

Microspectrometers for optical absorption spectroscopy have recently been introduced for composition measurement of gases and liquids. Microspectrometers based on tunable optical resonators are particularly suitable for narrowband operation, which conveniently aligns with the need in absorption spectroscopy for analyzing only the part of the spectrum closely around the absorption bands of the components of interest [1]. A highly interesting application is in composition analysis of combustible gases. Natural gas at a particular source has a fairly constant composition over time and an associated energy density as defined by its Wobbe index. However, increased international gas trade leads to natural gas mixtures of variable composition. Moreover, the trend toward the use of sustainable resources encourages the addition of biogas in the gas grid. These changes cause a non-constant gas composition and necessitate composition measurement for burner control at industrial facilities, gas distribution points, and households for safe and clean combustion [2]. These users combined constitute a high-volume application, which favors the use of a technique such as CMOS that offers costs advantages in batch fabrication [3]. The characteristic absorption lines of the hydrocarbons are in the mid-infrared (mid-infrared) spectral range between about 3.1 μm and 3.5 μm (Free Spectral Range, FSR = 400 nm at $\lambda_0 = 3300$ nm) and should be measured with a Full-Width Half-Magnitude resolution, FWHM, in the range between $\lambda_{\text{FWHM}} = 2$ and 5 nm for effective composition measurement [4].

A highly successful concept for narrowband spectroscopy in a CMOS microsystem is the Linearly Variable Optical Filter (LVOF) [5]. The LVOF is a one-dimensional array of many Fabry–Perot (FP)-type of optical resonators. Rather than a huge number of discrete devices, the LVOF has a center layer (the resonator cavity) in the shape of a strip and a thickness that changes over its length. Dielectric mirrors are on either side. Thus, the narrow passband wavelength of the LVOF varies linearly along its length, while the detector array that is positioned underneath the LVOF records the spectrum of the projected light. The tapered FP filter is fabricated directly on top of a detector array coated with the lower Bragg reflector composed of a dielectric layer stack, using low-temperature reflow of a specially patterned layer of resist on top of a resonator layer and the subsequent transfer etch into this intended resonator layer [5, 6]. Fabrication is completed with the deposition of the top Bragg mirror that is identical to the lower mirror design.

The specifications for natural gas composition measurement imply that the spectral separation between two adjacent maxima relative to the resolution, as expressed by the Finesse, $\mathfrak{F} = (\lambda_{0,m+1} - \lambda_{0,m})/m\lambda_{\text{FWHM}}$ in case of operation of the resonator in mode m , is in the range $660 < m\mathfrak{F} < 1650$. The feasibility of such a specification depends on the reflectivity that can be achieved with the optical materials in the dielectric layer stack in the Bragg reflector design, as expressed in the coefficient of Finesse, $F = 4R/(1-R)^2$. CMOS-compatible Bragg reflector design is limited by the use of CMOS-compatible materials and the number of optical layers in the filter, and the resonator should typically be operated at a higher mode. Operation at such a high order mode obviously reduces the relative spectral separation

between the adjacent maxima, which inevitably brings the challenge of suppressing the out-of-band orders of the resonator-based filter. This issue is well-known to high-Q filter design and is conventionally solved using additional layers in the multi-film quarter-lambda Bragg reflector design for the spectral selection of only the intended higher-order band [7]. The overall interference filter design with 60-80 dB out-of-band suppression requires a number of layers that significantly exceeds the acceptable number in a CMOS-compatible optical filter design and typically requires materials for a high index of refraction contrast and deposition techniques that are not compatible with silicon CMOS batch fabrication technology. Consequently, other techniques are needed.

Radiation in the mid-IR spectral range entering silicon does not lead to electron-hole pair generation by photon absorption, due to the indirect bandgap at 1.12 eV [8]. Therefore, a cascade of two transduction effects are typically used; first from impinging infrared radiation to heat generation, using an absorber, and subsequently from resulting temperature change to electrical signal using a thermo-electric effect. The absorption coefficient should be maximized for maximum sensitivity. However, the usual silicon-compatible materials do not offer opportunities for a design with high absorption in the mid-infrared. Approaches based on thin film interference filters using Ti or SiC [9–12], porous metal layers (gold black is best known [13–15], but also platinum black is reported [16]) and absorbers using areas coated with vertically grown carbon nanotubes (CNT) [17–19] are suitable for implementation in MEMS. These approaches typically result in wideband absorption, which is actually desirable in a pyrodetector.

Another highly promising category of absorbers is based on metamaterials. The metamaterial is a large array of unit cells with a fine structure within the cell that is engineered to provide resonance for an electromagnetic wave of well-defined wavelength. Mid-infrared metamaterial absorbers can be designed for near-perfect absorption within a specially designed spectrum. As the interaction between the impinging electromagnetic wave and a metamaterial primarily depends on energy absorption due to resonance, as defined by the shape of a pattern within a unit cell and the 2D arrangement of such cells, and not on the bulk material properties, the electric and magnetic response can be controlled by a specific design of the unit cell and an array structure, provided that the features within the cell are sub-wavelength. Consequently, absorbers for the mid-IR should be referred to as ‘large area’ devices, since a unit cell of μm^2 -dimensions with an inner pattern with sub- μm features is required over an absorber area of mm^2 [20, 21]. The spectral tuneability of the absorption by the structure within the unit cell enables a wavelength dependent response, which could be designed to contribute to the out-of-band suppression of a mid-IR microspectrometer, as is demonstrated in this work.

2. CMOS-compatibility design in mid-IR metamaterial absorbers

Metamaterial absorbers are mostly based on metal-insulator-metal (MIM) stacks, with the top metal patterned and the back-metal layer acting as a ground metal to ensure zero transmission. At normal incidence reflectance at the interface is $r = (Z - Z_0)/(Z + Z_0)$, where $Z = \sqrt{\epsilon/\mu}$ is the wavelength-dependent complex impedance of the medium and Z_0 is the impedance of free space. A near-unity absorbance is achieved when the impedance of the surface matches to that of the free-space ($Z = Z_0$), resulting in zero reflectance. The impedance of the metamaterial can be tuned by the dimensions and shape of the pattern and dielectric spacer in MIM structures. The resonating characteristic of metamaterials causes the impedance, Z , to strongly depend on the electromagnetic wave frequency, resulting in a typically narrow absorption band [20, 22]. A wider response can be achieved when incorporating several resonator structures in a staggered absorber unit-cell design [20, 23, 24].

The key challenges addressed here are: the additional constraints imposed by the CMOS-compatible processing for on-chip co-integration of the metamaterial with standard CMOS processing and MEMS fabrication, and the use of masked lithography in batch fabrication

that is common in microelectronic manufacturing to ensure acceptable throughput. There are three specific constraints: the first is the mandatory use of CMOS-compatible materials. Due to their high conductivity, gold (Au) and silver (Ag) have been the materials of choice as the plasmonic materials in most state-of-the-art metamaterials absorber designs [24, 25]. However, when considering CMOS-compatibility, the use of these materials greatly hinders the introduction of metamaterials in microfabricated systems. Aluminum (Al)-based metamaterial absorbers have been considered instead as a more CMOS-compatible approach for mid-IR metamaterial absorber design for the range between 3 and 4 μm . Al has been introduced in earlier works as a more-suitable CMOS-compatible candidate for mid-IR metamaterial absorbers, which demonstrate that a near perfect absorption can be achieved [26–28].

The second issue results from the use of masked lithography. A mid-infrared metamaterial design requires a sub-micron pattern resolution. Conventionally, high-resolution lithography methods, such as e-beam [22–25, 29–37], deep UV (DUV) [21], or direct laser write [38] lithography are used. However, the low throughput of e-beam lithography makes fabrication of relatively large-area devices time consuming, while DUV is prohibitively expensive. Therefore, the level of masked lithography that is a standard part of the infrastructure of a MEMS cleanroom (masked UV (i-line) lithography) has been explored for mid-infrared absorber fabrication. Analyzing literature on mid-infrared metamaterial-based absorbers reveals that the dividing line between e-beam fabricated, versus mask-fabricated devices is at the longer wavelength part of the IR spectrum [39–43]. For a typical mid-infrared design based on the cross and split-ring resonators, a feature size of about 80 nm (at 1 μm) [34] up to 400 nm (at 6 μm) [22] is required, which is beyond the specifications of masked UV lithography. In order to ease the fabrication requirements, the disk-shaped resonator is used in our study for its simpler geometry as compared to ring and cross resonators, while the lack of sharp features reduces the dependence on the limitations of masked lithography. The disk shape MIM structures have been previously implemented in the near and mid-infrared (e.g. [24, 29, 37, 43]). Extensive sensitivity analysis has also shown a relatively high tolerance of the disk fabrication to parameters such as the thickness of the spacer and pattern, and also the periodicity of the unit cell [26, 44].

The third constraint results from the acceptable techniques for metal layer deposition. The deposition should be at low temperature to be considered CMOS-compatible. However, the effect on surface roughness needs to be evaluated, as this property significantly affects the Q-factor of the absorber [27, 29]. Moreover, our earlier work has revealed that the increased scattering with surface roughness adversely affects the lithography [27]. The resulting deviations from the nominal dimensions cause a spectral shift and a widening of the absorption peak. The exposure dose sensitivity, on the other hand, results in a systematic error in the dimensions of the resulting pattern. It has been shown that for sub-resolution patterns, the fabrication results in a shift toward smaller patterns.

These considerations have been included in a four-band design of a metamaterial, which has been fabricated in a CMOS-compatible fashion over a large ($5 \times 5 \text{ mm}^2$) area using masked lithography. The CMOS-compatible fabrication of the metamaterial absorber facilitates the integration of metamaterial with sensor and readout circuits in CMOS. The performance is assessed with the three compatibility constraints in mind.

3. Design of a CMOS-compatible metamaterial absorber

Finite Element method was used to design the disk-shaped mid-infrared absorber. Lorentz-Drude model with $\omega_p = 2\pi \times 3.62 \times 10^3 \text{ THz}$ and $\gamma = 2\pi \times 19.2 \text{ THz}$ [45] was used for the aluminum layer, and a SiO_2 layer with a relative permittivity of 2.25 was used to model the dielectric spacer. Figure 1(a) shows the basic unit-cell design. A perfectly matched layer (PML) was used to back the radiation port and perfect electric conductor (PEC) and perfect magnetic conductor (PMC) boundary conditions were applied to the sides of the model

corresponding to a linear polarization. The S-parameter was then computed over the wavelength range of interest. Subsequently, the absorption was calculated ($A = 1 - R$).

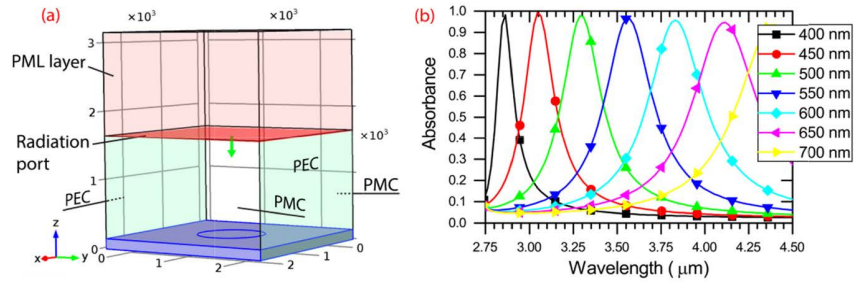


Fig. 1. (a) Unit-cell structure used in Finite Element analysis. (b). Absorption spectra for metamaterial structures with different disk radii as obtained using Finite Element simulations.

While the resonance wavelength is not significantly affected by variations in thickness or permittivity of the dielectric layer or periodicity of the unit cell, the choice for a nominal thickness of 160 nm and periodicity of 2.6 μm was found to result in maximum absorption [26]. Figure 1(b) shows the absorption peaks for different disk diameters as simulated using finite element model. Figure 2 shows the peak wavelength and FWHM of the disk metamaterials. The absorption peak is found to shift with the disk diameter by about 5 nm/nm, whereas the peak absorption does not vary significantly (see insert in Fig. 2). Accordingly, a disk diameter from about 800 nm up to 1300 nm is required to obtain an absorption peak in the range between 3 to 4 μm . The FWHM increases from about 200 nm from a peak wavelength at 3 μm up to about 500 nm at 4 μm .

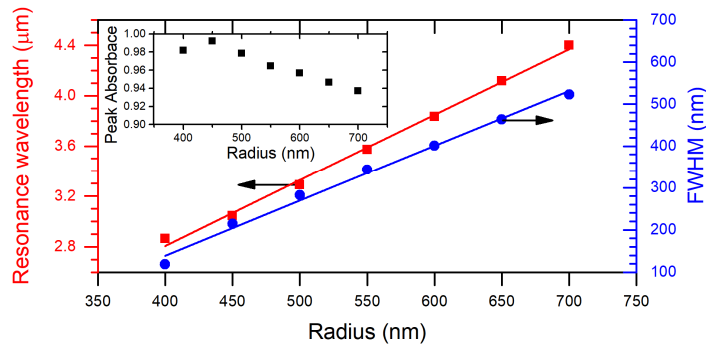


Fig. 2. Resonance wavelength and FWHM of absorbance peak for single disk resonator metamaterial absorbers as obtained using Finite Element simulation.

Figure 3 shows the electric and magnetic fields at the cross-section of the disks at the peak absorbance for a linearly polarized electromagnetic wave. Accordingly, the electric field is coupled strongly at the surface of the metallic disk and absorbed due to the ohmic loss. The localized surface plasmon oscillation in metal pattern and the anti-parallel surface current in the bottom metallic layer also induces a magnetic dipole inside the dielectric layer, absorbing the magnetic component of the incident field [43, 46].

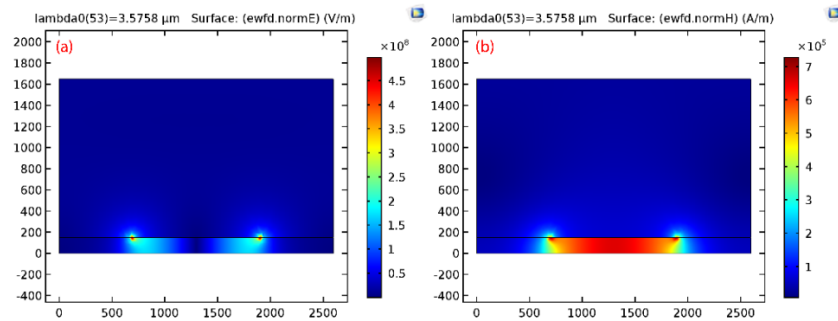


Fig. 3. (a) The electric field at E-plane shows the electric field enhancement at the edge of the disks. (b) The magnetic field at the H-plane; magnetic field resonance between the back metal and pattern.

A four-resonator metamaterial design, shown in Fig. 4(a), was used to obtain a wideband absorbance over the 3 to 4 μm spectral range. The disk radii in this wideband absorber are 0.480 μm , 0.495 μm , 0.545 μm , and 0.600 μm with a periodicity of 3.2 μm . Figure 4(b) shows the simulated absorption spectra for the multiplexed design. A tolerance of ± 20 nm in the radius of the disks is expected in the fabrication and analyzed here. This tolerance results in a shift of about 130 nm for the short-wavelength wing of the absorbance band and 100 nm for the long-wavelength wing.

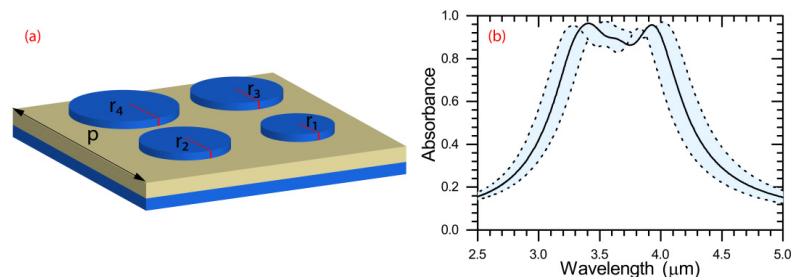


Fig. 4. (a) Schematic of the staggered metamaterial absorber; $p = 3200$ nm and r_1 to r_4 are 480 nm, 495 nm, 545 nm, and 600 nm respectively. (b) Simulated spectra for staggered resonators. The grayed area shows the ± 20 nm tolerance in disk radius.

4. Metamaterial absorber fabrication

As discussed in the previous section, the mid-infrared design requires a sub-micron pattern resolution, while conventional UV lithography (i-line) has been explored in this work. The minimum feature size of a typical mid-infrared absorber is typically less than the lithography resolution available in a MEMS foundry. Therefore, dedicated processing using CMOS-compatible materials of aluminum and SiO_2 is used here to fabricate metamaterials.

The fabrication process is shown schematically in Fig. 5. In the first step, 200 nm aluminum layer is sputtered on 4-inch silicon wafers with 500 nm thermally grown oxide. The thermal oxide layer is used to prevent the diffusion of aluminum into silicon and inducing surface roughness. Aluminum was sputtered at 25° C to obtain smaller grain size and hence lower roughness. The SiO_2 spacer layer was then deposited at 350° C using PECVD.

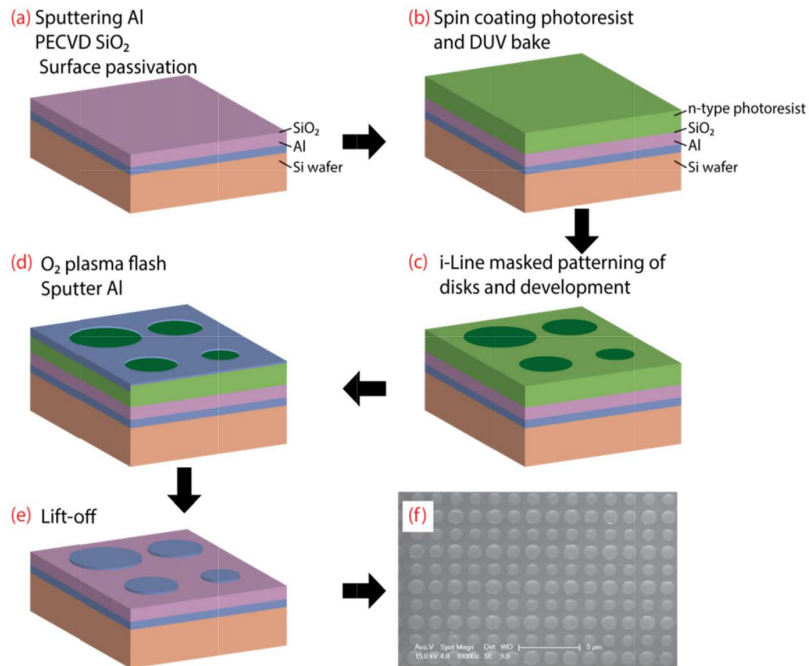


Fig. 5. Schematic of the fabrication process. (a) Deposition of the aluminum back reflector, SiO₂ spacer, and (b) photoresist spin coating. (c) Patterning of the photoresist with a negative mask. (d) O₂ Plasma flash and deposition of aluminum and (e) lift-off. A fabricated metamaterial structure is shown in (f).

Figure 6(a) shows the surface of the deposited spacer. The roughness average was measured to be $R_a = 30$ nm (measured using a stylus with a tip with radius of curvature $\rho = 2.5$ μm over a 500 μm long line). This high roughness value was found to be due to interactions between ions and the aluminum surface during PECVD. To protect the aluminum surface and decrease the roughness, the wafers were placed in 100% HNO₃ for 20 minutes to grow about 8 nm native oxide on the Aluminum layer (Fig. 6(b)). This results in a lower roughness $R_a = 6$ nm after deposition of PECVD SiO₂.

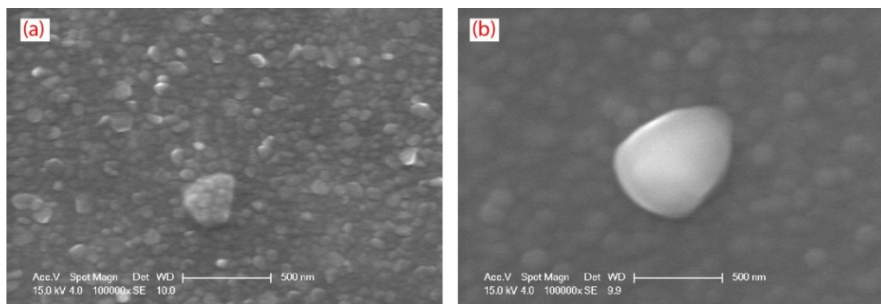


Fig. 6. Surface roughness after PECVD deposition of SiO₂ on Aluminum: (a) before the surface treatment in HNO₃ and (b) after. Some particles are also generated on the surface during the PECVD deposition.

A lift-off process was used to pattern the top metal layer with metamaterial design with a total area of 5×5 mm². A negative-tone photoresist film (1.5 μm; nLOF 2020) was spin-coated and patterned using a wafer stepper (ASML; PAS5500/80). The exposure dose was also varied from 40 to 44 mJ/cm². After the development of the photoresist, an O₂ plasma

flash step was used to clean the surface. An extended O_2 plasma etching was used to enlarge the patterns formed in photoresist due to its isotropic etch rate. Finally, after sputtering of a 60 nm aluminum at $25^\circ C$ and lift-off in NMP at $70^\circ C$ for 15 minutes with ultrasonic agitation, the metallic pattern is obtained.

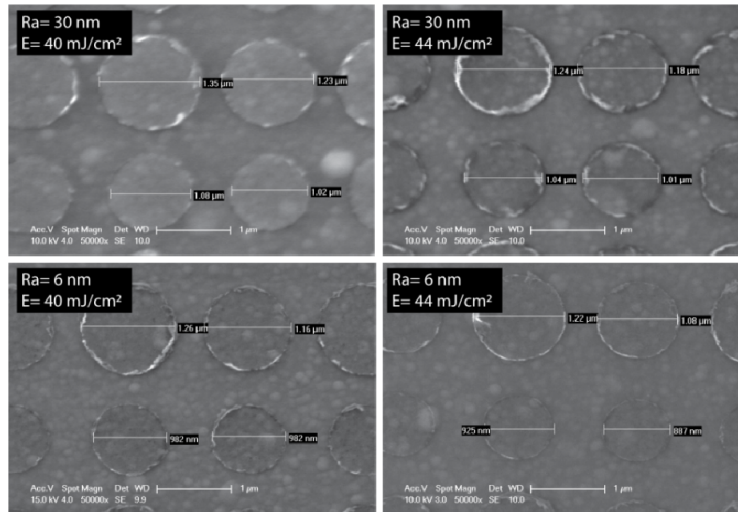


Fig. 7. SEM image of the fabricated metamaterial absorbers on SiO_2 spacer with no treatment ($R_a = 30$ nm) and with surface treatment ($R_a = 6$ nm). The exposure was varied from 40 to 44 mJ/cm^2 .

Figure 7 shows the variation of the radius of the disk by exposure dose and on different substrates. The scattering of UV light from the interface of the substrate during the lithography step resulting in a larger disk diameter for a same exposure dose on the rougher sample. Furthermore, increasing the exposure dose results in a decrease in the size of the disks. The analysis shows a sensitivity of diameter changes due to changes in exposure dose of -17 ± 2 nm/ $[mJ/cm^2]$. Tuning the exposure dose was used as a suitable parameter for obtaining the nominal dimensions. The dimensions of the disks fabricated on substrates with 6 nm roughness and an exposure dose of $44 mJ/cm^2$ are in good agreement with the nominal dimensions of the designed metamaterial absorber.

5. Measurements

The optical characterization of the samples was performed using an FTIR spectrometer (Bruker Vertex 70) equipped with a reflectance module. The large sample area (5×5 mm²) enables the optical characterization of the samples without the need for microscope FTIR. From the measurement of the reflectance at a well-defined angle of incidence, the spectral absorbance can be derived. A reflectance reference was used to normalize the measured spectrum. Figure 8(a) shows the measured spectral absorbance of the metamaterial absorbers on samples with different surface roughness at 12° incidence angle (which is the minimum setting due to equipment restrictions). The metamaterial absorber fabricated on the sample with a 30 nm roughness shows a slightly shifted absorption peak and also a higher out-of-band absorption. The peak absorbance is measured to be 98% with an absorbance of above 90% over the range of $3.5 \mu m$ to $4.1 \mu m$. Both figures confirm that the absorbance does not reduce to very low values at short wavelengths, because of the second-order resonance at about $2.2 \mu m$. As shown in Fig. 8(b) increasing the exposure dose shifts the peak into shorter wavelengths and closer to the simulation result. The measurement results for $44 mJ/cm^2$ is in good agreement with the simulation, reaching 94% absorption at $3.55 \mu m$.

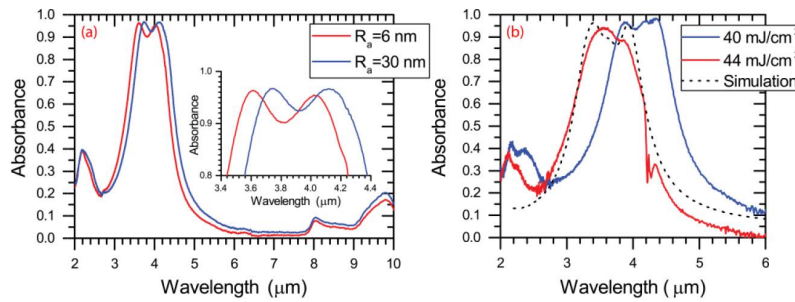


Fig. 8. Absorbance of samples with (a) surface roughness average of 6 nm and 30 nm and (b) with different exposure dose measured using FTIR at 12° incident angle.

The incident angle was varied from 12° to 60° , and the reflectance of the samples was measured. Figure 9 shows the absorbance contour spectra for the samples fabricated at different exposure doses as a function of the incidence angles up to 60° . In both cases, the absorbance remains almost undisturbed up to an incidence angle of 30° , while the peak absorbance decreases and the out-of-band absorption slightly increases at more oblique incidence. Figure 9(a) shows an absorption exceeding 90% over 600 nm wide band around a center wavelength of $4.1 \mu\text{m}$ is maintained up to 30 degrees for the 40 mJ/cm^2 sample. The 44 mJ/cm^2 sample, on the other hand, absorbs over 90% of the infrared light over a 300 nm band around a center wavelength of $3.55 \mu\text{m}$. The 90%-bandwidth decreases to about 200 nm for an incidence angle of 30° . Furthermore, measurements show that the out-of-band absorption remains well below 30% for incident angles up to 60° . The results correspond to about 20 dB suppression of absorption on the long infrared side.

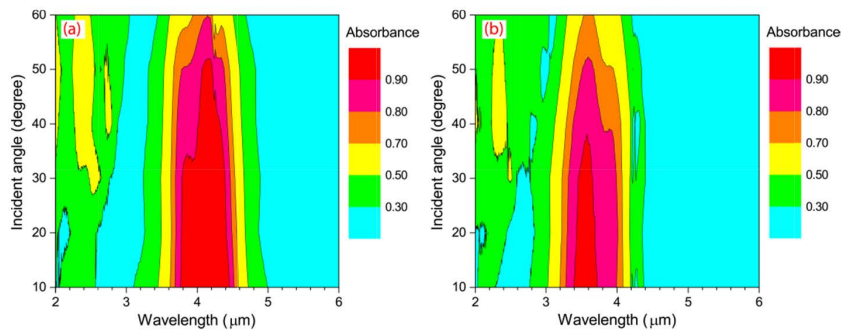


Fig. 9. The absorbance spectra contours as a function of the incident angle for a sample fabricated at (a) 40 mJ/cm^2 and (b) 44 mJ/cm^2 .

6. Conclusion

The masked fabrication used for enabling high throughput in CMOS batch fabrication inevitably also results in reduced resolution as compared to the e-beam lithography and thus reduces control over the features and results in deviations from the nominal dimensions for sub-resolution patterns. Irregularities in the shape and deviations from the nominal dimensions in a metamaterial structure result in uncertainties in absorber characteristics. The response of the metamaterial is averaged over the distribution of irregularities and errors over hundreds of unit structures. Therefore, while the structure is immune to the occasional fabrication defects, the statistical distribution of errors over a large area is the essential operational factor. Controlling the distribution of fabrication errors in masked based UV lithography is the main challenge.

Figure 10 shows the typical unit cell size per center wavelength for several state-of-the-art mid-IR metamaterial absorbers. The references are also labeled according to the fabrication

method, i.e. e-beam, standard UV, deep UV (DUV) and direct laser writing (DLW) lithography. There are two notable state-of-the-art metamaterial absorbers centered at mid-IR and fabricated using standard UV [40, 43]. Ogawa *et al.* [40] have used a plasmonic micrograting absorber (PMGA) to achieve wideband absorption by controlling the depth and tapering angle of the micrograting. Using this method, they were able to implement a larger unit cell and achieve wideband absorption for wavelengths as short as 4 μm . Yang *et al.* [43] used MIM structure with a layer of VO_2 in the dielectric spacer layer. By controlling the phase transition in VO_2 , a thermally tunable wideband absorption is achieved in the mid-IR using a relatively large pattern size (2.2 μm diameter disks, with a periodicity of 5 μm). Accordingly, e-beam lithography is still the prevailing method for devices operating at wavelengths lower than 5 μm . However, the techniques used in this work enabled us to use standard UV lithography in the wavelength range that has so far been dominated by e-beam lithography.

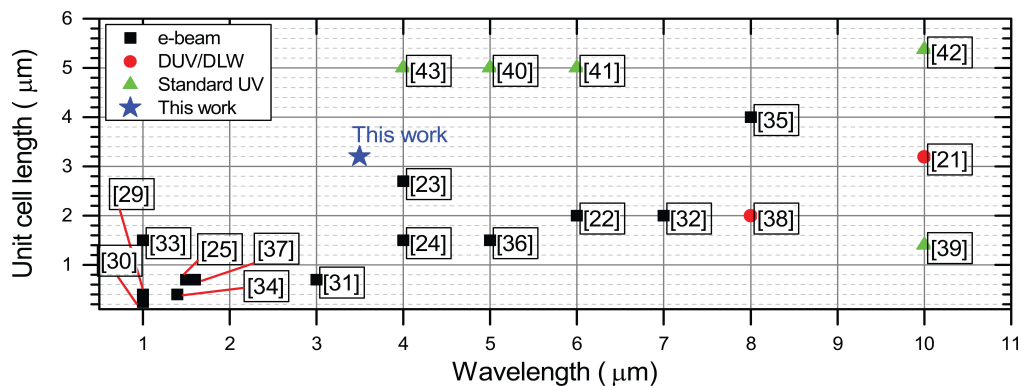


Fig. 10. The typical unit-cell and center wavelength for the state of the art mid-infrared metamaterial absorbers, fabricated using e-beam [22-25, 29-37], standard UV [39-43], Deep UV (DUV) [21], and direct laser writing (DLW) [38] lithography methods. The metamaterial structure presented in this paper is also shown for comparison. (note that for wideband absorbers the shortest wavelength is listed).

The design and fabrication process was optimized to facilitate CMOS-compatible fabrication of large-area mid-IR absorbers using standard masked UV lithography. The size of the fabricated sub-resolution disks depends strongly on both the exposure dose and the surface roughness of the samples. The surface roughness was found to be an important source of error in the fabrication of sub-resolution features sizes. In our samples, a similar exposure dose on samples with $R_a=6$ nm and 30 nm roughness resulted in larger patterns on the rougher surface and a 100 nm shift of absorption spectra. The exposure dose on the other hand results in a systematic error in feature sizes, hence was used as an effective parameter to tune the process. We measured about -17 ± 2 nm/(mJ/cm²) variations in diameter due to exposure variation.

The throughput advantage of masked lithography has been exploited for the fabrication of mid-IR absorbers over an area of 5×5 mm² and the measurement confirmed the theoretical spectral response. A peak absorption of 98% at center wavelength of 4.1 μm and 94% at 3.55 μm for an angle close to perpendicular incidence was observed. The absorption exceeded 90% over 300 nm range for the absorber centered at 4.1 μm and over 200 nm range for the peaks at 3.55 μm respectively. Furthermore, measurements at an angle of incidence up to 60° show that the absorption characteristics of the metamaterials are maintained for incidence angles below 30°. The fabricated metamaterials resulted in about 20 dB suppression of absorbance at longer wavelengths. Future work is aiming on the integration of mid-IR metamaterials in microspectrometers for gas sensing.

Acknowledgment

The authors would like to thank the staff of EKL (DIMES) of Delft University of Technology for their support during fabrication.